assumed to depend on force but not time. $k_{-2}(f) = 2k_{-1}(f/2)$ because the force on a dimeric bond is shared equally by the two subunits, each of which behaves as a monomeric bond and is equally likely to dissociate. k_{+2} is assumed to be a constant. The monomeric model predicts that lifetimes are distributed exponentially. Performing a log–linear plot renders the exponential distribution linear; thus $-k_{-1}$ equals the slope of the ln(number of events with a lifetime of t or more) against t plot. Also, $\langle t \rangle_1 = \sigma_1(t) = 1/k_{-1}$. By comparison, the dimeric model predicts that

$$\langle t \rangle_2 = (1 + k_{+2}/k_{-2})/k_{-1} + 1/k_{-2}$$

and

$$\sigma_2(t) = \{[(1 + k_{+2}/k_{-2})/k_{-1} + 1/k_{-2}]^2 - 2/(k_{-1}k_{-2})\}^{1/2}$$

The $k_{-1}(f)$ values that allow the monomeric model to fit the data in Fig. 3a also allow the dimeric model to fit the data in Fig. 3b.

Lifetimes measured in a flow chamber

Lifetimes of transient tethers of neutrophils and microspheres were measured in flow-chamber experiments as described in refs 12 and 19. Neutrophils were isolated from healthy donors. Polystyrene microspheres (6 μm diameter; Polysciences, Warrington, Pennsylvania) either precoated or not with streptavidin were incubated with biotinylated sPSGL-1 or mAb G1. Neutrophils or microspheres were perfused at various wall shear stresses over dimeric P-selectin or monomeric sP-selectin adsorbed at low densities on the chamber floor. The tethers were eliminated by coating the floor with human serum albumin instead of (s)P-selectin or by the inclusion of the anti-P-selectin mAb G1, the anti-PSGL-1 mAb PL1 or EDTA in the medium, confirming their specificity. The force f on the tether of a neutrophil or a microsphere was calculated on the basis of the tether angle, which was derived after directly measuring the lever arm of the tether by a flow reversal method[19]. The conversion factors between wall shear stress and tether force for neutrophils and microspheres are 112 and 131 pN dyn^{-1} cm^{-2}, respectively. Five sets of lifetimes (~100 tether events in each set) were measured for each interaction at each wall shear stress. Each set was analysed by the plot of ln(number of events with a lifetime of t or more) against t, which was fitted by a straight line. The correlation coefficients, R^2, were more than 0.9 for all 200 fits. The −1/slope values of the fits were plotted against the wall shear stress (points in Fig. 4b). The difference in mean −1/slope values at any two neighbouring wall shear stresses was statistically significant ($P < 0.05$, Student's t-test), except occasionally at the beginning of the slip bond regime after transition from the catch bond regime.

Received 11 November 2002; accepted 19 February 2003; doi:10.1038/nature01605.

1. Vestweber, D. & Blanks, J. E. Mechanisms that regulate the function of the selectins and their ligands. *Physiol. Rev.* **79,** 181–213 (1999).
2. McEver, R. P. & Cummings, R. D. Perspectives series: cell adhesion in vascular biology. Role of PSGL-1 binding to selectins in leukocyte recruitment. *J. Clin. Invest.* **100,** 485–491 (1997).
3. McEver, R. P. Adhesive interactions of leukocytes, platelets, and the vessel wall during hemostasis and inflammation. *Thromb. Haemost.* **86,** 746–756 (2001).
4. Bell, G. I. Models for the specific adhesion of cells to cells. *Science* **200,** 618–627 (1978).
5. Dembo, M., Tourney, D. C., Saxman, K. & Hammer, D. The reaction-limited kinetics of membrane-to-surface adhesion and detachment. *Proc. R. Soc. Lond. B* **234,** 55–83 (1988).
6. Dembo, M. *Lectures on Mathematics in the Life Sciences, Some Mathematical Problems in Biology* 51–77 (American Mathematical Society, Providence, Rhode Island, 1994).
7. Alon, R., Hammer, D. A. & Springer, T. A. Lifetime of the P-selectin–carbohydrate bond and its response to tensile force in hydrodynamic flow. *Nature* **374,** 539–542 (1995).
8. Pierres, A., Benoliel, A. M., Bongrand, P. & van der Merwe, P. A. Determination of the lifetime and force dependence of interactions of single bonds between surface-attached CD2 and CD48 adhesion molecules. *Proc. Natl Acad. Sci. USA* **93,** 15114–15118 (1996).
9. Alon, R., Chen, S., Puri, K. D., Finger, E. B. & Springer, T. A. The kinetics of L-selectin tethers and the mechanics of selectin-mediated rolling. *J. Cell Biol.* **138,** 1169–1180 (1997).
10. Chen, S. & Springer, T. A. An automatic braking system that stabilizes leukocyte rolling by an increase in selectin bond number with shear. *J. Cell Biol.* **144,** 185–200 (1999).
11. Smith, M. J., Berg, E. L. & Lawrence, M. B. A direct comparison of selectin-mediated transient, adhesive events using high temporal resolution. *Biophys. J.* **77,** 3371–3383 (1999).
12. Ramachandran, V. *et al.* Dimerization of a selectin and its ligand stabilizes cell rolling and enhances tether strength in shear flow. *Proc. Natl Acad. Sci. USA* **98,** 10166–10171 (2001).
13. Chen, S. & Springer, T. A. Selectin receptor–ligand bonds: Formation limited by shear rate and dissociation governed by the Bell model. *Proc. Natl Acad. Sci. USA* **98,** 950–955 (2001).
14. Merkel, R., Nassoy, P., Leung, A., Ritchie, K. & Evans, E. Energy landscapes of receptor–ligand bonds explored with dynamic force spectroscopy. *Nature* **397,** 50–53 (1999).
15. Finger, E. B. *et al.* Adhesion through L-selectin requires a threshold hydrodynamic shear. *Nature* **379,** 266–269 (1996).
16. Lawrence, M. B., Kansas, G. S., Kunkel, E. J. & Ley, K. Threshold levels of fluid shear promote leukocyte adhesion through selectins (CD62L,P,E). *J. Cell Biol.* **136,** 717–727 (1997).
17. Geng, J.-G. *et al.* Rapid neutrophil adhesion to activated endothelium mediated by GMP-140. *Nature* **343,** 757–760 (1990).
18. Moore, K. L. *et al.* The P-selectin glycoprotein ligand from human neutrophils displays sialylated, fucosylated, O-linked poly-*N*-acetyllactosamine. *J. Biol. Chem.* **269,** 23318–23327 (1994).
19. Yago, T. *et al.* Distinct molecular and cellular contributions to stabilizing selectin-mediated rolling under flow. *J. Cell Biol.* **158,** 787–799 (2002).
20. Moore, K. L. *et al.* P-selectin glycoprotein ligand-1 mediates rolling of human neutrophils on P-selectin. *J. Cell Biol.* **128,** 661–671 (1995).
21. Moore, K. L., Varki, A. & McEver, R. P. GMP-140 binds to a glycoprotein receptor on human neutrophils: evidence for a lectin-like interaction. *J. Cell Biol.* **112,** 491–499 (1991).
22. Chen, S., Alon, R., Fuhlbrigge, R. C. & Springer, T. A. Rolling and transient tethering of leukocytes on antibodies reveal specializations of selectins. *Proc. Natl Acad. Sci. USA* **94,** 3172–3177 (1997).
23. Ushiyama, S., Laue, T. M., Moore, K. L., Erickson, H. P. & McEver, R. P. Structural and functional characterization of monomeric soluble P-selectin and comparison with membrane P-selectin. *J. Biol. Chem.* **268,** 15229–15237 (1993).
24. Fritz, J., Katopodis, A. G., Kolbinger, F. & Anselmetti, D. Force-mediated kinetics of single P-selectin/ligand complexes observed by atomic force microscopy. *Proc. Natl Acad. Sci. USA* **95,** 12283–12288 (1998).
25. Leppänen, A., White, S. P., Helin, J., McEver, R. P. & Cummings, R. D. Binding of glycosulfopeptides to P-selectin requires stereospecific contributions of individual tyrosine sulfate and sugar residues. *J. Biol. Chem.* **275,** 39569–39578 (2000).
26. Somers, W. S., Tang, J., Shaw, G. D. & Camphausen, R. T. Insights into the molecular basis of leukocyte tethering and rolling revealed by structures of P- and E-selectin bound to SLe(X) and PSGL-1. *Cell* **103,** 467–479 (2000).
27. Isberg, R. R. & Barnes, P. Dancing with the host; flow-dependent bacterial adhesion. *Cell* **110,** 1–4 (2002).
28. Hutter, J. L. & Bechhoefer, J. Calibration of atomic-force microscope tips. *Rev. Sci. Instrum.* **64,** 1868–1873 (1993).
29. McConnell, H. M., Watts, T. H., Weis, R. M. & Brian, A. A. Supported planar membranes in studies of cell–cell recognition in the immune system. *Biochim. Biophys. Acta* **864,** 95–106 (1986).
30. Wong, J. Y. *et al.* Polymer-cushioned bilayers. I. A structural study of various preparation methods using neutron reflectometry. *Biophys. J.* **77,** 1445–1457 (1999).

Acknowledgements We thank V. Moy for providing the AFM design and training. This work was supported by grants from the National Institutes of Health.

Competing interests statement The authors declare that they have no competing financial interests.

Correspondence and requests for materials should be addressed to C.Z. (cheng.zhu@me.gatech.edu).

Folding at the speed limit

Wei Yuan Yang* & Martin Gruebele*†

** Center for Biophysics and Computational Biology, and † Departments of Chemistry and Physics, University of Illinois, Urbana Illinois 61801, USA*

Many small proteins seem to fold by a simple process explicable by conventional chemical kinetics and transition-state theory. This assumes an instant equilibrium between reactants and a high-energy activated state[1]. In reality, equilibration occurs on timescales dependent on the molecules involved, below which such analyses break down[1]. The molecular timescale, normally too short to be seen in experiments, can be of a significant length for proteins. To probe it directly, we studied very rapidly folding mutants of the five-helix bundle protein λ_{6-85}, whose activated state is significantly populated during folding. A time-dependent rate coefficient below 2 μs signals the onset of the molecular timescale, and hence the ultimate speed limit for folding[2]. A simple model shows that the molecular timescale represents the natural pre-factor for transition state models of folding.

The pre-factor $\nu^\dagger$, together with the activation energy $\Delta G^\dagger$, determines the rate coefficient $k = \nu^\dagger \exp(-\Delta G^\dagger/kT)$ of transition state theory. For small molecules, $\nu^\dagger \approx kT/h \approx (0.2\,\mathrm{ps})^{-1}$ is a reasonable value. Proteins are simply too large to move about and fold in a fraction of a picosecond. Protein folding pre-factors have been estimated on the basis of random intramolecular collision within small peptide loops, yielding $\nu^\dagger \approx$ 10–100 ns (refs 3–6). This number might be too small for the molecular timescale of larger proteins. Their backbone and side chains can collide in more ways and with more non-additive interactions, introducing additional roughness into the free-energy landscape. A calculation for the five-helix bundle protein λ_{6-85} has yielded numbers closer to 0.5 μs (refs 7, 8), and evidence from unfolded cytochrome c in denaturant indicates values in the 1–40-μs range[9]. Single-molecule experiments have put an upper limit of 200 μs on the pre-factor[10].

This range of pre-factors leaves us with an ambiguity that has so far precluded the determination of protein folding barriers from experiment: many combinations of $\nu^\dagger$ and $\Delta G^\dagger$ yield the same

observable rate coefficient k. Without sufficient knowledge of the critical reaction coordinates for describing the motions represented by $\nu^{\dagger}$, it is impossible to relate experimentally determined folding rates rigorously to computed free-energy barriers.

We provide direct evidence that the molecular timescale of λ_{6-85} is 2 μs, by observing relaxation towards equilibrium induced by a fast temperature jump induced by a laser[11]. Rigorous kinetic theory has shown that the rate coefficient increases from its phenomenological value once the molecular timescale is reached[1]. Below about 4 μs, such a speed-up beyond exponential kinetics occurs for our fastest-folding mutants. Slower-folding proteins have barriers that are too high to reveal the depletion of activated populations, and show perfect single-exponential kinetics. We analyse our results in terms of numerical diffusion calculations with a simple one-dimensional two-well model, whose renormalized diffusion coefficient accounts for traps and reduced dimensionality. (Models with explicit traps also fit the data; see Supplementary Information and ref. 12.)

The wild type and many mutants of the 80-residue amino-terminal λ repressor fragment λ_{6-85} (including sites Asp 14, Gln 33, Ala 37, Gly 46 and Gly 48 (refs 13–15), and T. Oas, personal communication) have been studied by Oas and co-workers. They introduced the Tyr22Trp mutation as a fluorescence probe that shifts spectrally from 334 to 355 nm after the unfolding and solvent exposure of the protein core[14]. An NMR line shape analysis[13] and stopped-flow measurements[14] in denaturant solutions both revealed rates that extrapolated to less than 20 μs for the fastest mutants in the absence of any denaturant.

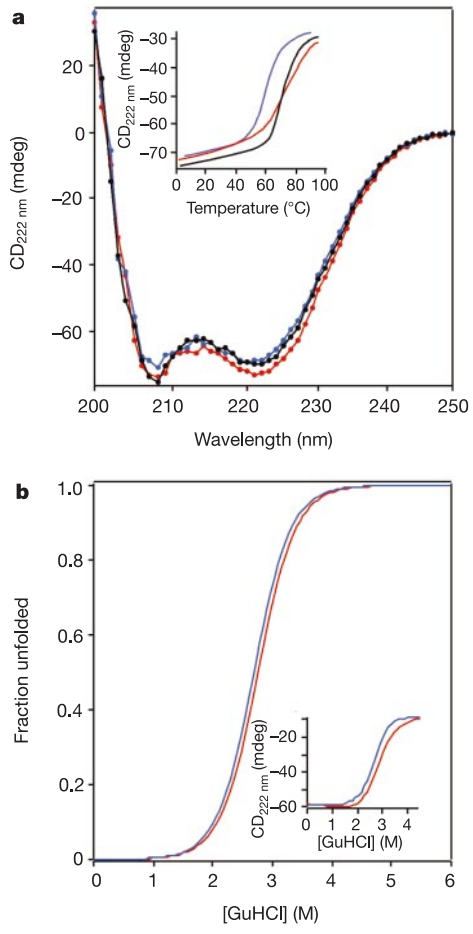

Figure 1 Spectroscopy of mutant proteins. **a**, Circular dichroism (CD) signatures of the three λ_{6-85} mutants (20 °C, 5 μM, 1-cm cuvette): λQ33Y (red), λD14A (black) and λA37G (blue). Inset: sigmoidal temperature titration curves. **b**, Unfolded population fits on guanidinium chloride (GuHCl) titration data (assuming that the free energy is linearly dependent on guanidinium chloride concentrations) taken by circular dichroism at 222 nm (red) and fluorescence at 280 nm (blue). Inset: raw data. Baseline-corrected population fits show at most small deviations of the transition midpoint by different measurement techniques.

Such fast folding makes λ_{6-85} an ideal starting point for creating even faster mutants to reach the speed limit. Unlike NMR studies, our temperature-jump experiments can be performed with nanosecond resolution under very favourable folding conditions without denaturant. All our proteins contained the mutations Tyr22Trp and Gln33Tyr. The Tyr 33/Trp 22 pair introduces an aromatic interaction that speeds up folding and provides a large Trp fluorescence-lifetime change after unfolding. The three distinguishing sets of mutations were: Gly46Ala/Gly48Ala, which speeds up folding by stabilizing helix 4; Asp14Ala/Gly46Ala/Gly48Ala, an additional mutation that removes a hydrogen bond between positions 14 and 77; and Ala37Gly, a model for slower folding because helix 4 is not stabilized and helix 3 is destabilized instead. We abbreviate these mutants below as λQ33Y, λD14A and λA37G (see Methods).

The three variants had helical contents very similar to the wild type, judging from their circular dichroism spectra (Fig. 1a). Thermal denaturation occurs by means of sigmoidal transitions of the circular dichroism and fluorescence spectra between 1 and 95 °C, confirming apparent two-state thermodynamic behaviour (Fig. 1a inset). The unfolded states are exposed to solvent and have largely lost helical structure. Denaturant titration (Fig. 1b) reveals at most a small displacement between different spectroscopic probes.

In the kinetics experiments, laser temperature jumps from 9–20 °C to a series of final temperatures were applied to initiate relaxation (see Methods). Relaxation to the new equilibrium constant was monitored by tryptophan fluorescence lifetimes. The excellent signal-to-noise ratio allowed us to measure relaxation rates even under folding conditions, with final equilibrium constants $K > 20$. The kinetics of λA37G was the slowest ($k_a \approx 50$ μs), and fitted well to a single exponential under all experimental conditions (Fig. 2c). The faster-folding λQ33Y and λD14A are single-exponential only at $t > 4$ μs. Their relaxation transients speed up beyond the main relaxation phase below 4 μs. This very fast phase grows to more than 20% of the total signal under the most favourable folding conditions (lowest temperatures, Fig. 2a, b). λQ33Y relaxation is fairly well fitted by a double exponential (Figs 2a and 3a), indicating that there is still some separation of timescales in the underlying dynamics. The even faster λD14A data are better fitted by a stretched exponential $\exp(-kt)^{\beta}$, with $\beta = 0.72 \pm 0.02$ (Fig. 2b), indicating a merger of the two timescales as folding becomes faster. For easy comparison, Fig. 3a reports double-exponential fits of k_m (molecular rate coefficient) and k_a (activated rate coefficient) for all proteins, and Fig. 3b shows activated folding rate coefficients k_f.

The origin of the swift initial decay is of particular interest because the transient lies in the bracket between 10 ns and 40 μs set for the molecular timescale by peptide-diffusion[3,4], unfolded-protein[9,16] and single-molecule experiments[10]. The initial decay speeds up the kinetics when optimal folding conditions are approached, as predicted by rigorous rate theory[1]. It is an 'anti-rollover' of the folding rate, not a slow-down caused by a rate-limiting folding intermediate. The data cannot be globally fitted to a model involving a conventional early intermediate (see Supplementary section 2). The ratio of the fast to the main phase does not increase when the temperature-jump size is increased from 9 to 20 °C. λA37G has no fast phase, so equilibration in the folded and unfolded well, which should occur in slow proteins also, is ruled out as the sole source of the signal. The fast mutants have no fast phase when jumped from one native condition to another, ruling out equilibration within the folded well as the only cause. For the fastest mutants, the main folding phase is slowed down at high concen-

trations by aggregation[17] (Fig. 2d). We therefore operate in the low-concentration limit ([λA37G] < 300 μM, [λQ33Y] < 100 μM and [λD14A] < 40 μM), where the main folding phase has converged to its fastest value, in accord with a previous model[17]. The lower concentration thresholds of the fastest mutants indicate partly unfolded populations. This could be because partly folded preactivated conformations are already populated in the lowest barrier mutants, and interact in quantity upon collision.

Having excluded other reasonable explanations, we assign the fast phase to the increase in speed beyond phenomenological kinetics predicted by theory below the molecular timescale[1]. A one-dimensional two-well model can account for all the observed kinetic and thermodynamic trends of all three mutants as a function of temperature (Fig. 4; see Methods and Supplementary Information). In this model, a low barrier supports both a preactivated subpopulation that reacts on the very fast molecular timescale, as well as a main population that reacts on the activated timescale. Higher barriers (slower-folding proteins) yield only the activated single-exponential relaxation signal of conventional two-state models.

Simulations were performed by equilibrating populations with the use of Langevin dynamics in the high friction limit, then applying a jump to the potential and monitoring population re-equilibration (see Methods and Supplementary Information). To reproduce the molecular and activated phases and their relative amplitudes, the effective diffusion constant must be decreased to 1.6×10^{-4} nm^2 ns^{-1}, and the barrier is very low for the fast mutants (Fig. 4).

Because we can observe both the molecular-timescale k_m^{-1} and activated kinetics in one measurement, we can devise a useful equation for the activation energy. The molecular rate constant k_m in Fig. 3 reflects the average time that proteins spend in the activated region and can therefore be related to the slower activated rate constant k_a by

$$k_a/k_m = \exp(-G_{act}/kT) \quad (1)$$

This equation is an operational definition of barrier size in terms of the energetically accessible phase space in the activated as opposed to the well regions of the free energy. Thus, a very broad higher barrier can have the same population as a lower narrower

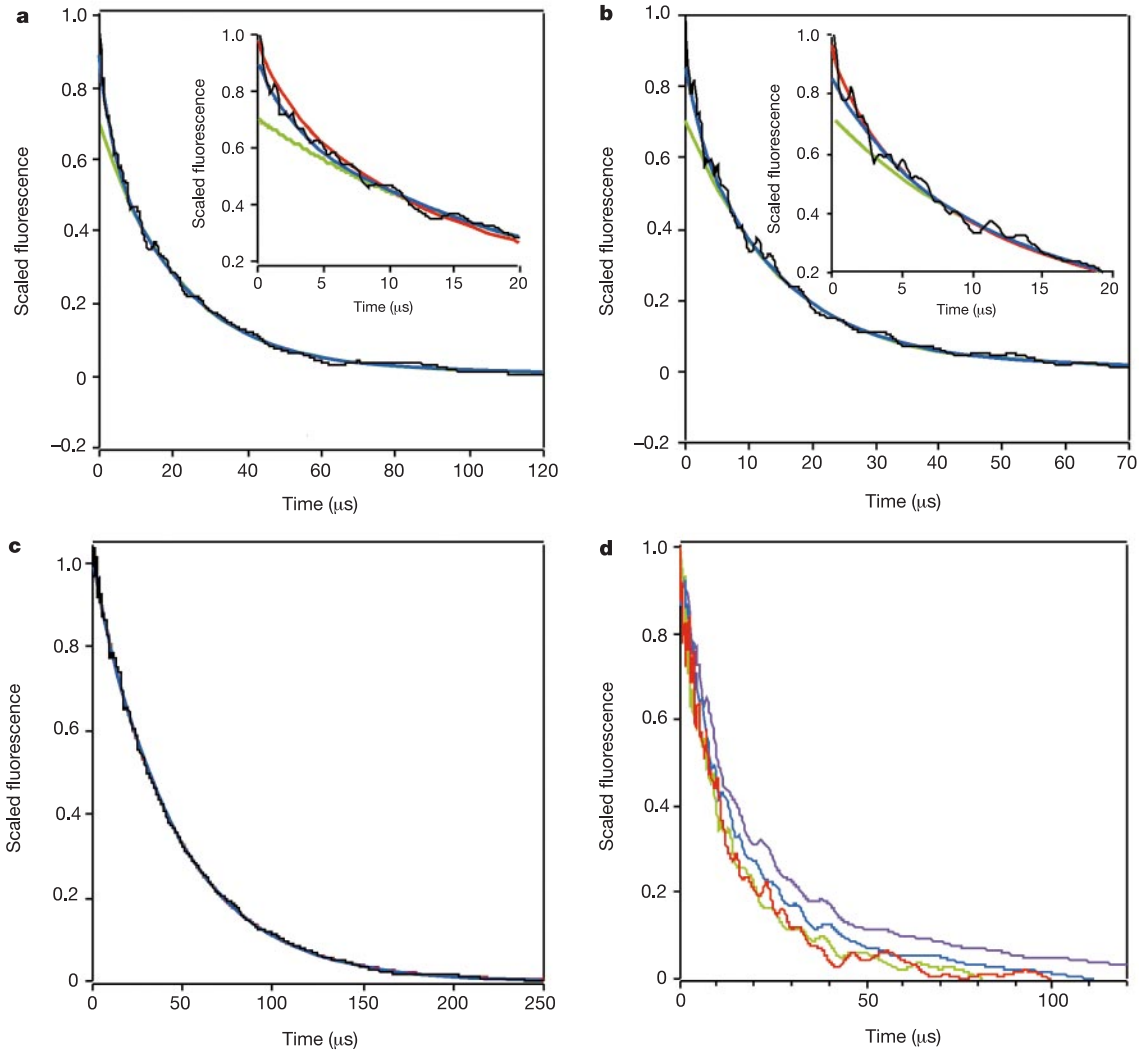

Figure 2 Relaxation after temperature jumps. **a**, Relaxation of λQ33Y at 63 °C (black curve). Blue curve, double exponent; green curve, long time exponent. Inset: detailed view near $t = 0$. A stretched exponential (red; $\beta = 0.74 \pm 0.02$) performs comparably to a double-exponential fit (black). The best overall exponential fit (blue) and long-time exponential fit (green, slow component of double exponential fit) are also shown, and deviate markedly from experiment. **b**, As in **a**, for λD14A at 61 °C. Here the stretched-exponential fit ($\beta = 0.72 \pm 0.02$) performs slightly better than the double-exponential fit. **c**, The slower λA37G mutant at 56 °C (black curve) fits to a single exponential (blue curve), even when the stretching factor β is allowed to vary ($\beta = 0.96 \pm 0.04$). The fast mutants both require $\beta < 0.8$. **d**, Transient aggregation slows the relaxation at high concentrations of λD14A, at 61 °C. Below 40 μM (for λD14A) and 100 μM (for λQ33Y; see Supplementary Information), the relaxation converges to a maximum rate reflecting the collision-free folding reaction. Red curve, 15 μM; green curve, 31 μM; blue curve, 95 μM; purple curve, 173 μM.

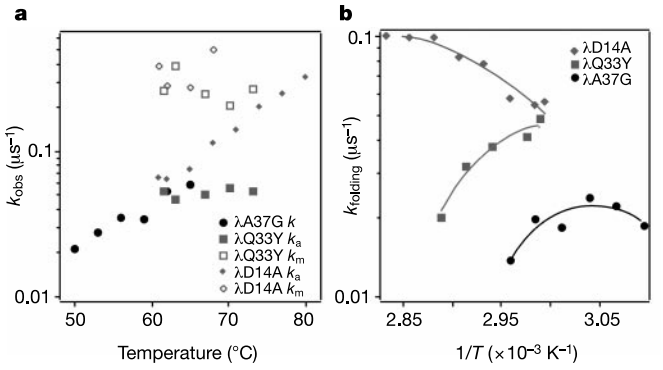

Figure 3 Rate coefficient determination. **a**, Single-exponential and double-exponential fits to the experimental relaxation data. Two rate coefficients (k_m, molecular; k_a, activated) are shown for the fast mutants, and one (k_a) for the slow mutant. The separation of timescales ranges from only 4 to 8 for λD14A and λQ33Y. **b**, Activated folding rates computed from k_a and the known equilibrium constants K (Fig. 1) from $k_f = k_a K/(K+1)$. Quadratic activation energy fits are shown. The fast mutants behave very differently from one another, with the slow mutant showing intermediate turnover behaviour (see Supplementary Information).

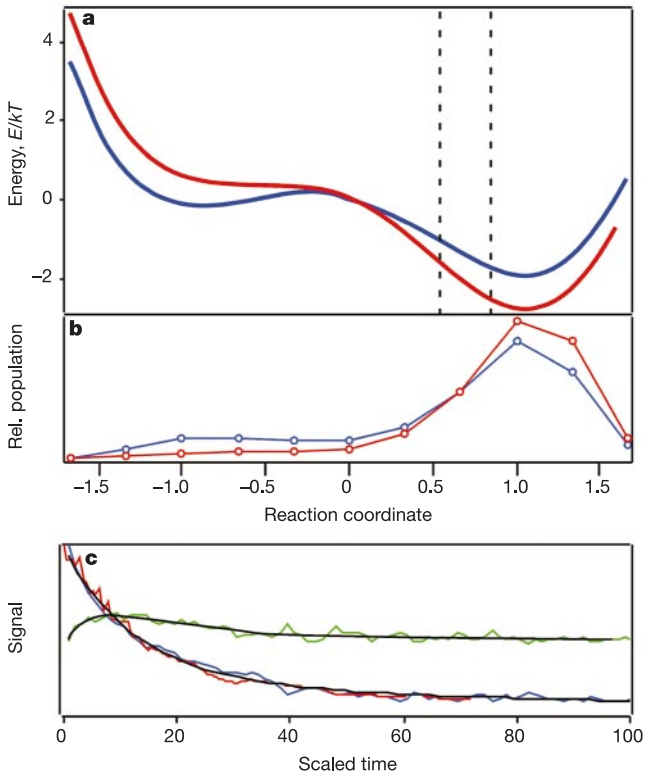

Figure 4 One-dimensional free-energy model used to reproduce the λQ33Y and λD14A data as a function of temperature. **a**, Double-well surface before (red) and after (blue) temperature jump to 63 °C; vertical bins mark where the fluorescence signal switches from unfolded to native in the model. **b**, Binned equilibrated protein populations before and after the jump, showing sizeable activated populations. **c**, Population (green line) and double-exponential fit (black curve) for the bin in **a**, and λQ33Y experimental kinetics (red line), simulated fluorescence signal (blue line) and double-exponential fit (black curve). The relative rates and amplitudes fit λD14A at 63 °C (and at all other temperatures (not shown); see Supplementary Information); the absolute rates are matched by adjusting the diffusion constant in the Langevin equation (see the text).

barrier. Our definition, based on the separation of experimental timescales, yields $G_{act} \approx \ln(8.3)kT \approx 2.1kT$ for λQ33Y at 60 °C, and $G_{act} \approx \ln(4.5)kT \approx 1.5kT$ for λD14A at 65 °C. The value $1.5kT$ lies outside the range of validity of activated rate models. Previously, only partial downhill folding and thermodynamic signs for barrier-free folding were observed[18,19].

Why is the $k_m^{-1} \approx 2\,\mu s$ molecular timescale slower than the measured 50-ns loop closure time for unfolded peptides? When an 80-residue protein folds, it undergoes multiple 50-ns contact formations and rearrangements along the reaction coordinate: it has a broad, rough activated region. Broad-barrier models, and also dimpled-barrier models—which lump all the roughness into one state (see Supplementary Information)—have been proposed[20,21]. A more realistic picture is that the barrier region contains a distribution of local minima, the deepest of which can be classified as intermediates. Such a picture has been found[7,8], with multiple mini-transition states from an analytical folding model for λ_{6-85}. A prefactor for backbone dynamics of about 0.5 μs has been calculated for the wild-type protein under favourable folding conditions, in good agreement with our measured molecular timescale[7,8]. Our renormalized diffusion constant of about 1.6×10^{-4} nm^2 ns^{-1} (compared with about 0.05 nm^2 ns^{-1} in inter-chain diffusion measurements[9]) mimics an even distribution of traps and landscape roughness, and corrects for the reduced dimensionality of the model. A $4.7kT$ trap and 0.007 nm^2 ns^{-1} diffusion constant must be invoked to account for the roughness in a dimpled-barrier model (see Supplementary Information).

The speed limit for λ_{6-85} is 2 μs. Whether this is ascribed to a renormalized diffusion constant, a single trap or multiple local minima along an explicitly computed reaction coordinate depends on the level of theory chosen. A barrier size given by the ratio of the molecular to the activated timescale (equation (1)) is a more robust descriptor for protein folding than the barrier height and curvature usually chosen for small molecules. Fortunately, analytical theory[7], and now a direct comparison of experimental folding kinetics and molecular dynamics simulations[22], avoid over-reliance on phenomenological rate models. However, simulations must exceed the molecular timescale to determine rate coefficients reliably. For very small proteins, a nanosecond timescale is probably sufficient[22], but larger proteins evidently require about 1 μs or longer before phenomenological rate equations can be applied. Finally, fast folding phases of some smaller proteins, interpreted more conventionally in terms of unfolded states under native conditions or folding intermediates[23], need careful further investigation in view of the results and models outlined here. □

Methods

Experimental

The gene encoding λ_{6-85} was a gift from T. Oas. It was inserted into the PET-15b vector, tagging the protein with six histidine residues followed by a thrombin cleavage site at the N terminus. Mutations were carried out using the Quickchange site-directed mutagenesis kit (Stratagene). Proteins were expressed in BL21(DE3) and purified through a Ni^{2+}-nitrilotriacetate and a Sephacryl S-200 HR column (Pharmacia). Thrombin was used to remove the hexahistidine tag. The final λ-repressor used in the measurements contained three extra residues (Gly-Ala-Met) at the N terminus of the wild-type sequence. All measurements were done in 50 mM potassium phosphate buffer, pH 7. Concentrations were determined assuming an extinction coefficient of 8,200 cm^{-1} M^{-1} at 280 nm. Circular dichroism spectra were taken at 5 μM protein concentration, fluorescence spectra at 1 μM. The melting points of the mutants were 60 °C for λA37G, 71 °C for λQ33Y and 74 °C for λD14A. Kinetics were monitored by exciting tryptophan at 288 nm every 14 ns with a mode-locked, frequency-tripled Ti:S laser. The total fluorescence was filtered through a 320–380-nm bandpass filter, imaged onto a 500-ps rise-time photomultiplier tube, and digitized every 0.5 ns. Scaled fluorescence was calculated by fitting the fluorescence decay shape as $f(t) = \chi_1 f_1 + (1-\chi_2) f_2$, where f_1 is the initial fluorescence profile just after the temperature jump and f_2 is the fluorescence profile after equilibration. This yields a single exponential only when a two-state model applies; otherwise it deviates from single-exponential behaviour[24]. Magnitudes of phases can be compared quantitatively as a function of temperature, but not between mutants because of innate differences in the fluorescence profiles. We have engineered a low-stability variant containing mutations Ala37Gly/Ala49Gly in addition to Tyr22Trp that can be denatured by cold. It can be both refolded (from the cold-denatured state at subzero temperatures) and unfolded (from the folded state at high temperatures) with folding rates differing only by the ratio of the water viscosity at the two temperatures. Because water viscosity has a

large inherent dependence on temperature, we concluded that the folding reaction is at least near the Kramers high friction limit.

Computational

The double-well potential used was $g(x) = x^4 - 2x^2$. Temperature effects were treated as a linear bias along the reaction coordinate, $t(x,T) = A(T)x$, where $A(T)$ is an adjustable parameter for matching the equilibrium data. The folded and unfolded states are separated by 2 distance units along the reaction coordinate, corresponding to a typical helix diffusion length when taken to be nanometres. The population at $x < 0.83$ was assumed to have the same fluorescence signature as the unfolded state, and at $x > 0.83$ as the folded state (for compatibility with the three-well model in the Supplementary Information, any value $x > 0$ yields the same qualitative result). Fluorescence was simulated by convolving populations (for example Fig. 4b) with this response. The one-dimensional Langevin equation with gaussian white noise was integrated by using a fourth-order Runge–Kutta method. A time-step size of 0.01 was used in the integration, and time steps were scaled to match the experimentally observed absolute kinetics. Similar calculations for a three-well model that also matches the data are described in the Supplementary Information.

Received 24 January; accepted 31 March 2003; doi:10.1038/nature01609.

1. Berne, B. J. in *Activated Barrier Crossing: Applications in Physics, Chemistry and Biology* (eds Hänggi, P. & Fleming, G. R.) 82–119 (World Scientific, Singapore, 1993).
2. Hagen, S. J., Hofrichter, J., Szabo, A. & Eaton, W. A. Diffusion-limited contact formation in unfolded cytochrome c: Estimating the maximum rate of protein folding. *Proc. Natl Acad. Sci. USA* **93,** 11615–11617 (1996).
3. Lapidus, L. J., Eaton, W. A. & Hofrichter, J. Measuring the rate of intramolecular contact formation in polypeptides. *Proc. Natl Acad. Sci. USA* **97,** 7220–7225 (2000).
4. Bieri, O. *et al.* The speed limit for protein folding measured by triplet–triplet energy transfer. *Proc. Natl Acad. Sci. USA* **96,** 9597–9601 (1999).
5. Yeh, I. C. & Hummer, G. Peptide loop-closure kinetics from microsecond molecular dynamics simulations in explicit solvent. *J. Am. Chem. Soc.* **124,** 6563–6568 (2002).
6. Thirumalai, D. Time scales for the formation of the most probable tertiary contacts in proteins with applications to cytochrome C. *J. Phys. Chem. B* **103,** 608–610 (1999).
7. Portman, J. J., Takada, S. & Wolynes, P. G. Microscopic theory of protein folding rates. II. Local reaction coordinates and chain dynamics. *J. Chem. Phys.* **114,** 5082–5096 (2001).
8. Portman, J. J., Takada, S. & Wolynes, P. G. Microscopic theory of protein folding rates. I. Fine structure of the free energy profile and folding routes from a variational approach. *J. Chem. Phys.* **114,** 5069–5081 (2001).
9. Hagen, S. J., Hofrichter, J. & Eaton, W. A. Rate of intrachain diffusion of unfolded cytochrome c. *J. Phys. Chem. B* **101,** 2352–2365 (1997).
10. Schuler, B., Lipman, E. A. & Eaton, W. A. Probing the free-energy surface for protein folding with single-molecule fluorescence spectroscopy. *Nature* **419,** 743–747 (2002).
11. Gruebele, M., Sabelko, J., Ballew, R. & Ervin, J. Laser temperature jump induced protein refolding. *Acc. Chem. Res.* **31,** 699–707 (1998).
12. Metzler, R., Klafter, J. & Jortner, J. Hierarchies and logarithmic oscillations in the temporal relaxation patterns of proteins and other complex systems. *Proc. Natl Acad. Sci. USA* **96,** 11085–11089 (1999).
13. Burton, R. E., Huang, G. S., Daugherty, M. A., Calderone, T. L. & Oas, T. G. The energy landscape of a fast-folding protein mapped by Ala → Gly substitutions. *Nature Struct. Biol.* **4,** 305–309 (1997).
14. Ghaemmaghami, S., Word, J. M., Burton, R. E., Richardson, J. S. & Oas, T. G. Folding kinetics of a fluorescent variant of monomeric lambda represssor. *Biochemistry* **37,** 9179–9185 (1998).
15. Myers, J. M. & Oas, T. G. Contribution of a buried hydrogen bond to lambda repressor folding kinetics. *Biochemistry* **38,** 6761–6768 (1999).
16. Chang, I. J., Lee, J. C., Winkler, J. R. & Gray, H. B. The protein-folding speed limit: intrachein diffusion times set by electron transfer rates in denatured $Ru(NH_3)_5$(His-33)-Zn-cytochrome c. *Proc. Natl Acad. Sci. USA* **100,** 3838–3840 (2003).
17. Silow, M. & Oliveberg, M. Transient aggregates in protein folding are easily mistaken for folding intermediates. *Proc. Natl Acad. Sci. USA* **94,** 6084–6086 (1997).
18. Sabelko, J., Ervin, J. & Gruebele, M. Observation of strange kinetics in protein folding. *Proc. Natl Acad. Sci. USA* **96,** 6031–6036 (1999).
19. Garcia-Mira, M. M., Sadqi, M., Fischer, N., Sanchez-Ruiz, J. M. & Muñoz, V. Experimental identification of downhill protein folding. *Science* **298,** 2191–2195 (2002).
20. Silow, M. & Oliveberg, M. High-energy channeling in protein folding. *Biochemistry* **36,** 7633–7637 (1997).
21. Pappenberger, G., Saudan, C., Becker, M., Merbach, A. E. & Kiefhaber, T. Denaturant-induced movement of the transition state of protein folding revealed by high-pressure stopped-flow measurements. *Proc. Natl Acad. Sci. USA* **97,** 17–22 (2002).
22. Snow, C. D., Nguyen, H., Pande, V. S. & Gruebele, M. Absolute comparison of simulated and experimental protein-folding dynamics. *Nature* **420,** 102–106 (2002).
23. Mayor, U. *et al.* The complete folding pathway of a protein from nanoseconds to microseconds. *Nature* **421,** 863–867 (2003).
24. Ervin, J., Sabelko, J. & Gruebele, M. Submicrosecond real-time fluorescence detection: application to protein folding. *J. Photochem. Photobiol. B* **54,** 1–15 (2000).

Supplementary Information accompanies the paper on **www.nature.com/nature**.

Acknowledgements We thank T. Oas for suggesting many helpful lambda repressor mutations. This work was supported by an Alumni Scholarship and a Camille Dreyfus Teacher–Scholar Award to M.G.

Competing interests statement The authors declare that they have no competing financial interests.

Correspondence and requests for materials should be addressed to M.G. (gruebele@scs.uiuc.edu).

erratum

Antibody neutralization and escape by HIV-1

Xiping Wei, Julie M. Decker, Shuyi Wang, Huxiong Hui, John C. Kappes, Xiaoyun Wu, Jesus F. Salazar-Gonzalez, Maria G. Salazar, J. Michael Kilby, Michael S. Saag, Natalia L. Komarova, Martin A. Nowak, Beatrice H. Hahn, Peter D. Kwong & George M. Shaw

Nature **422**, 307–312 (2003).

In the seventh panel of Fig. 2 of this Letter, the V5 sequence of clone 391-3 appeared incorrectly as: SEKDQTEIFRP. It should read: SKDNQTEIFRP. In addition, there should be no yellow shading (indicating a change in glycosylation) for this sequence. □

corrigenda

Synaptic depression in the localization of sound

Daniel L. Cook, Peter C. Schwindt, Lucinda A. Grande & William J. Spain

Nature **421**, 66–70 (2003).

It has come to our attention that we failed to cite a relevant study[1] in our Letter. These authors identified the mechanism of synaptic depression measured at the embryonic chick nucleus magnocellularis to nucleus laminaris synapse as primarily presynaptic, which justifies the synaptic depletion model we used. Furthermore, the narrowing of coincidence detection time windows with EPSP depression as they observed may contribute to the adaptive mechanisms that we described. □

1. Kuba, H., Konomi, K. & Ohmori, H. *Eur. J. Neurosci.* **15,** 984–990 (2002).

Short interfering RNA confers intracellular antiviral immunity in human cells

Leonid Gitlin, Sveta Karelsky & Raul Andino

Nature **418**, 430–434 (2002).

In Fig. 5a of this Letter, the first and third panels (untreated and siL-treated cells, respectively) should not be identical: the correct figure is shown here. □